



Elastic envelope inversion using multicomponent seismic data without low frequency

C. Huang et al.

Elastic envelope inversion using multicomponent seismic data without low frequency

C. Huang, L. Dong, Y. Liu, and B. Chi

State Key Laboratory of Marine Geology, Tongji University, Shanghai 20092, China

Received: 6 November 2014 – Accepted: 7 November 2014 – Published: 5 December 2014

Correspondence to: L. Dong (dlg@tongji.edu.cn)

Published by Copernicus Publications on behalf of the European Geosciences Union & the American Geophysical Union.

Title Page

Abstract

Introduction

Conclusions

References

Tables

Figures



Back

Close

Full Screen / Esc

Printer-friendly Version

Interactive Discussion



Abstract

Low frequency is a key issue to reduce the nonlinearity of elastic full waveform inversion. Hence, the lack of low frequency in recorded seismic data is one of the most challenging problems in elastic full waveform inversion. Theoretical derivations and numerical analysis are presented in this paper to show that envelope operator can retrieve strong low frequency modulation signal demodulated in multicomponent data, no matter what the frequency bands of the data is. With the benefit of such low frequency information, we use elastic envelope of multicomponent data to construct the objective function and present an elastic envelope inversion method to recover the long-wavelength components of the subsurface model, especially for the S-wave velocity model. Numerical tests using synthetic data for the Marmousi-II model prove the effectiveness of the proposed elastic envelope inversion method, especially when low frequency is missing in multicomponent data and when initial model is far from the true model. The elastic envelope can reduce the nonlinearity of inversion and can provide an excellent starting model.

1 Introduction

Over the past several decades, the oil and gas exploration industry has been making great efforts to use full waveform inversion (FWI) to achieve high-resolution quantitative subsurface models by exploiting full information contained in prestack seismic data. However, most applications of FWI to real data have been performed under acoustic approximation. In practice, there is a simultaneous recording of the complicated elastic effects during seismic wave propagation in subsurface media, such as shear-wave reflections, converted waves and amplitude offset variations. Therefore, acoustic FWI suffers from limitations due to the acoustic approximation and may lead to erroneous models if applied to elastic data without specific data preprocessing and inversion preconditions (Brenders and Pratt, 2007; Brossier et al., 2009). Meanwhile, quantitative

Elastic envelope inversion using multicomponent seismic data without low frequency

C. Huang et al.

Title Page

Abstract

Introduction

Conclusions

References

Tables

Figures



Back

Close

Full Screen / Esc

Printer-friendly Version

Interactive Discussion



imaging of the elastic properties of the subsurface is essential for oil and gas-reservoir characterization because elastic parameter quantification can be used to deduce the lithology, fluid content and pore pressure of rocks (Tatham and Stoffa, 1976). Hence, elastic full waveform inversion (EFWI) is urgently required.

Up to now, only a few applications of EFWI have been presented. Aside from the computational challenges, EFWI is a highly ill-posed and nonlinear problem. It is sensitive to the quality of data, the accuracy of starting model and the frequency band of seismic data (Virieux and Operto, 2009). To make things worse, multiparameter EFWI is more ill-conditioned than acoustic FWI because different parameters are more or less coupled and the propagation of the elastic wave is more complicated than acoustic wave.

It is well known that low frequency is essential to reduce the nonlinearity of FWI, and the lack of ultra-low frequency (frequency below 2 Hz) in seismic data leads to difficulty in recovering the long-wavelength components of subsurface model and increases the starting-model dependence of FWI (Virieux and Operto, 2009). To reduce the starting-model dependence, multiscale inversion has been developed (Bunks et al., 1995; Pratt et al., 1996, 1998; Sirgue and Pratt, 2004; Fichtner and Tranpert, 2011; Baeten et al., 2013). Multiscale inversion is a strategy to mitigate the local minimum problem in FWI by starting from the lowest frequency to the highest frequency available in data. Brossier et al. (2009) also pointed out that the short S-wavelength could increase the nonlinearity of EFWI and more accurate starting models or lower frequency was required to reach convergence. However, ultra-low frequency is not always available in real seismic data, which is one of the main reasons causing failure when applying multiscale inversion strategy in either time domain or frequency domain.

To overcome the lack of low frequency issue in FWI, some other forms of FWI methods are developed by introducing different objective function instead of waveform. For example, Luo and Schuster (1991) used first-arrival traveltimes as matching objects and applied cross-correlation to measure the time difference. Zhang et al. (2011) extended this method to update the deep part of subsurface model by using reflection data.

Elastic envelope inversion using multicomponent seismic data without low frequency

C. Huang et al.

Title Page

Abstract

Introduction

Conclusions

References

Tables

Figures

◀

▶

◀

▶

Back

Close

Full Screen / Esc

Printer-friendly Version

Interactive Discussion



Elastic envelope inversion using multicomponent seismic data without low frequency

C. Huang et al.

Title Page

Abstract

Introduction

Conclusions

References

Tables

Figures

◀

▶

◀

▶

Back

Close

Full Screen / Esc

Printer-friendly Version

Interactive Discussion

step inversion strategy. For the first step, elastic envelope inversion is implemented to recover the long-wavelength components of subsurface models to obtain acceptable background models. Then, these elastic envelope inversion results are used as the starting models for conventional EFWI to recover the short-wavelength components of subsurface models. Final results are presented to show the validity of this inversion strategy.

2 Methodology

2.1 Objective function, gradient operator and the adjoint sources for elastic envelope inversion

The EFWI is based on the following second-order linear elastic wave equation system

$$\rho \partial_t^2 \mathbf{u} - \nabla \cdot \boldsymbol{\sigma} = \mathbf{f} \quad (1)$$

$$\boldsymbol{\sigma} = \mathbf{C} : \nabla \mathbf{u}$$

$$\mathbf{C} = \begin{pmatrix} C_{11} & \cdots & C_{16} \\ \vdots & \cdots & \vdots \\ C_{16} & \cdots & C_{66} \end{pmatrix}, \quad (2)$$

where ρ stands for the density, $\mathbf{u} = (u_x, u_y, u_z)^\top$ and $u_j (j = x, y, z)$ is the j th component of the particle displacement \mathbf{u} . $\boldsymbol{\sigma} = (\sigma_{xx}, \sigma_{yy}, \sigma_{zz}, \sigma_{yz}, \sigma_{xz}, \sigma_{xy})^\top$ and σ_{ij} is the stress tensor. $C_{ij} (i, j = 1, \dots, 6)$ is the Hooke tensor and \mathbf{f} is the source term. In order to simplify the computation, here we consider the media as isotropic and the density is known. It is easy to apply such method into other media if needed.

The objective function for conventional EFWI is generally defined as

$$J(\mathbf{m}) = \frac{1}{2} \sum_{s,r} \int_0^T [u(\mathbf{x}_s, \mathbf{x}_r, t; \mathbf{m}) - \mathbf{d}(\mathbf{x}_s, \mathbf{x}_r, t)]^2 dt, \quad (3)$$

and the objective function of elastic envelope inversion is defined as

$$J_{e1}(\mathbf{m}) = \frac{1}{2} \sum_{s,r} \int_0^T [E_u^p(\mathbf{x}_s, \mathbf{x}_r, t; \mathbf{m}) - E_d^p(\mathbf{x}_s, \mathbf{x}_r, t)]^2 dt, \quad (4)$$

where $\mathbf{u}(\mathbf{x}_s, \mathbf{x}_r, t; \mathbf{m})$ and $\mathbf{d}(\mathbf{x}_s, \mathbf{x}_r, t)$ are synthetic and observed particle displacements respectively at given source \mathbf{x}_s and receiver \mathbf{x}_r . In order to simplify the formula, we replace $\mathbf{u}(\mathbf{x}_s, \mathbf{x}_r, t; \mathbf{m})$ and $\mathbf{d}(\mathbf{x}_s, \mathbf{x}_r, t)$ with \mathbf{u} and \mathbf{d} for short. E_u is the envelope of simulated displacement vector \mathbf{u} defined by $E_{u_j} = \sqrt{u_j^2 + \tilde{u}_j^2}$ ($j = x, y, z$) with \tilde{u}_j being the Hilbert transform of u_j . E_d is the envelope of the multicomponent seismic data \mathbf{d} defined by $E_{d_j} = \sqrt{d_j^2 + \tilde{d}_j^2}$ ($j = x, y, z$) with \tilde{d}_j being the Hilbert transform of d_j . p is the power for the envelope data and can be any positive number.

In the time domain, higher power p means heavier weight on the energetic arrivals (Wu et al., 2014). Our numerical tests also show that, if we put $p > 1$, it will diminish most of the later arrivals of multicomponent data and the inversion cannot penetrate to the deep zone. Therefore, we set $p = 1$ throughout this paper.

From the defined elastic envelope objective function (Eq. 4), we can get the corresponding gradient operator and the adjoint source by the adjoint-state approach, a way of computing a gradient of an objective functional depending on recursive simulations (Plessix, 2006; Brossier, 2009; Chavent, 2009; Pessix and Cao, 2011; Gholami et al., 2013). Considering compressional-wave speed V_p and shear-wave speed V_s as the model parameters, the gradient of the misfit function with respect to V_p and V_s can be

Elastic envelope inversion using multicomponent seismic data without low frequency

C. Huang et al.

Title Page

Abstract

Introduction

Conclusions

References

Tables

Figures

◀

▶

◀

▶

Back

Close

Full Screen / Esc

Printer-friendly Version

Interactive Discussion



obtained by

$$\begin{aligned}
 \nabla_m J_{e1} &= \sum_{s,r} \int_0^T \left[E_u^p - E_d^p \right] \frac{\partial E_u^p}{\partial \mathbf{m}} dt \\
 &= \rho \sum_{s,r} \int_0^T \left[E_u^p - E_d^p \right] \sqrt{\mathbf{u}^2 + \tilde{\mathbf{u}}^2}^{p-2} \left(\mathbf{u} \frac{\partial \mathbf{u}}{\partial \mathbf{m}} + \tilde{\mathbf{u}} \frac{\partial \tilde{\mathbf{u}}}{\partial \mathbf{m}} \right) dt \\
 &= \rho \sum_{s,r} \int_0^T \left\{ \left[E_u^p - E_d^p \right] E_u^{p-2} \mathbf{u} - H \left\{ \left[E_u^p - E_d^p \right] E_u^{p-2} \tilde{\mathbf{u}} \right\} \right\} \frac{\partial \mathbf{u}}{\partial \mathbf{m}} dt
 \end{aligned} \tag{5}$$

where $H\{\}$ indicates the Hilbert transform and $\mathbf{m} = \begin{pmatrix} V_p \\ V_s \end{pmatrix}$. From Eq. (5), we can infer that the form of the gradient operator for this elastic-envelope inversion remains the same with the conventional EFWI, only the adjoint source changes. Thus, we can express the gradients with respect to V_p and V_s as (Liu and Tromp, 2006)

$$\nabla_{V_p} J_{e1}(\mathbf{x}) = -2\rho V_p \int_0^T \nabla \mathbf{u}^+(\mathbf{x}, T-t) \cdot \nabla \mathbf{u}(\mathbf{x}, t) dt, \tag{6}$$

and

$$\nabla_{V_s} J_{e1}(\mathbf{x}) = -4\rho V_s^2 \int_0^T \mathbf{D}^+(\mathbf{x}, T-t) : \mathbf{D}(\mathbf{x}, t) dt + \frac{8}{3}\rho V_s \int_0^T \nabla \mathbf{u}^+(\mathbf{x}, T-t) \cdot \nabla \mathbf{u}(\mathbf{x}, t) dt. \tag{7}$$

Here

$$\begin{cases} \mathbf{d} = \frac{1}{2}[\nabla \mathbf{u} + (\nabla \mathbf{u})^T] - \frac{1}{3}(\nabla \cdot \mathbf{u})\mathbf{I} \\ \mathbf{d}^+ = \frac{1}{2}[\nabla \mathbf{u}^+ + (\nabla \mathbf{u}^+)^T] - \frac{1}{3}(\nabla \cdot \mathbf{u}^+)\mathbf{I} \end{cases}, \tag{8}$$

Elastic envelope inversion using multicomponent seismic data without low frequency

C. Huang et al.

Title Page

Abstract

Introduction

Conclusions

References

Tables

Figures

◀

▶

◀

▶

Back

Close

Full Screen / Esc

Printer-friendly Version

Interactive Discussion



and \mathbf{I} is identical matrix. \mathbf{u}^+ stands for the adjoint elastic wavefield, which is the solution of Eq. (1) with the adjoint sources ($p = 1$)

$$\mathbf{f}^+ = \mathbf{u} \left\{ \frac{\mathbf{E}_u - \mathbf{E}_d}{\mathbf{E}_u} \right\} - H \left\{ \frac{\mathbf{E}_u - \mathbf{E}_d}{\mathbf{E}_u} \tilde{\mathbf{u}} \right\}. \quad (9)$$

Chi et al. (2014) and Wu et al. (2014) both mentioned the demodulation effect of the envelope operator in acoustic FWI. And elastic envelope operator also works efficiently in retrieving ultra-low frequency from standard multicomponent seismic records even when the data is filtered out by a high-pass filter. In the next section, we shall focus on the role of such low frequency data playing in reducing the nonlinearity of elastic envelope inversion.

2.2 The advantage of elastic envelope misfit function

Elastic full waveform inversion is an ill-posed, nonlinear problem even for apparently simple models involving few parameters. Low frequency is a key issue to reduce the nonlinearity of EFWI, but mostly it is missing in real seismic data. In Eq. (4), we introduce the elastic envelope objective function. The envelope is extracted from the waveform data by a square-root operator. The square-root operator is a nonlinear operator and can be treated as a nonlinear filter. Hence, the envelope operator is equivalent to a demodulation operator: if we treat the seismogram as a modulated signal, the low-frequency envelope is the modulation signal and the high-frequency reflection waveforms are the carrier signal. And that is the superiority of envelope misfit function to conventional misfit function, which gives us a way to overcome the low frequency issue in EFWI.

To test the ability of the elastic envelope operator in retrieving low frequency from seismic signal, a rick wavelet signal and its envelope are plotted in Fig. 1. By comparing their spectra, strong ultra-low frequency can be found in the envelope of wavelet but not shown in the wavelet itself. More complicate signals are presented in Fig. 2 to

Elastic envelope inversion using multicomponent seismic data without low frequency

C. Huang et al.

[Title Page](#)

[Abstract](#)

[Introduction](#)

[Conclusions](#)

[References](#)

[Tables](#)

[Figures](#)

[⏪](#)

[⏩](#)

[◀](#)

[▶](#)

[Back](#)

[Close](#)

[Full Screen / Esc](#)

[Printer-friendly Version](#)

[Interactive Discussion](#)



further test the envelope operator. An elastic shot gather is shown in Fig. 2a and b for the horizontal and vertical components of partial displacement from the synthetic data set of 2-D Marmousi-2 model (see the numerical tests section for more details). Their envelope data are plotted in Fig. 3 and the corresponding spectra are presented in Fig. 4. It is easy to notice that the envelope data have stronger ultra-low frequency and weaker high frequency comparing with the original waveform. Even when we filter the data below 5 Hz out from the original waveform (Fig. 5), the main energy of the corresponding envelope (Fig. 6) is still laid in ultra-low frequency zone (Fig. 7). With the benefit of ultra-low frequency in envelope, we can well recover the low-wavenumber components of subsurface model, hence to reduce the nonlinearity of elastic envelope inversion.

Gradient in EFWI determines the direction of the model updating. Next, a simple test is made to illustrate the superiority of the elastic envelope gradient to conventional gradient. The reference model is homogeneous with the P-velocity 1.5 km s^{-1} and S-velocity 0.9 km s^{-1} respectively. A homogeneous circular inclusion is buried in the center, whose radius is 200 m, P-velocity is 4.0 km s^{-1} and S-velocity is 2.5 km s^{-1} (Fig. 8). The density is kept constant being 2.1 kg m^{-3} . All receivers are laid along four boundaries of the reference model and 40 explosive shots using a rick wavelet with dominant frequency of 8 Hz are fired uniformly along the four boundaries. The frequency of all synthetic records below 6 Hz have been filtered out. The starting model is the reference model without inclusion and the gradient of the first iteration is presented in Fig. 9. The gradient of conventional EFWI only reveals the boundary of the inclusion, especially for V_s , while the gradient of elastic envelope provides not only the boundary information, but more inner part information of the inclusion. It means that without low frequency, the conventional EFWI gradient shall fail to image the inner part of the inclusion and the inversion result will fall into a local minimum. Conversely, because of the ultra-low frequency, the gradient of the envelope objective function performs better in inverting the inner part of the inclusion and may help the inversion avoid the local minimum problem.

can greatly reduce the nonlinearity of EFWI and decrease the dependence on the starting model.

In order to test the sensitivity of the objective functions to the low-frequency components in the data, we redo the 2-D canonical test by filtering the synthetic data below 6 Hz. The results are shown in Fig. 12. As expected, the envelope misfit function behaves more stable than the waveform misfit function. It means that elastic envelope inversion is less influenced by low frequency issue existed in conventional EFWI.

2.4 The derivation of low frequency information in elastic envelope of multicomponent data

Due to the robust performance on retrieving low frequency from multicomponent data, the elastic envelope objective function is superior to waveform objective function to recover the background of subsurface model. But if the collected multicomponent data contains no low frequency information, where the low frequency information comes from in the corresponding envelope? In acoustic envelope FWI, Wu et al. (2014) presented an approximate formula to show how the low frequency comes from, and in elastic envelope inversion, we can also derive an approximate formula below for multicomponent data (see Appendix A for more details).

$$E^2(u_i(t)) \approx \left(G_{ik}^f(t)\right)^2 \left[(s_k(t))^2 + \{H[s_k(t)]\}^2\right] + \left(\mathbf{G}_{ik}^{sr}(t)\right)^2 \left[(\mathbf{y}_k(t))^2 + \{H[\mathbf{y}_k(t)]\}^2\right], \quad (10)$$

$$= \left(G_{ik}^f(t)\right)^2 E^2(s_k(t)) + \left(\mathbf{G}_{ik}^{sr}(t)\right)^2 E^2(\mathbf{y}_k(t))$$

where $\mathbf{s}(t)\{s_k(t), k = x, y, z\}$ is the wavelet function applied at position \mathbf{x}_s . G_{ik}^f is the Green's function for the direct arrival, $\mathbf{y}(\mathbf{x}) = \begin{pmatrix} \gamma^{\text{pp}}(\mathbf{x}) & \gamma^{\text{sp}}(\mathbf{x}) \\ \gamma^{\text{ps}}(\mathbf{x}) & \gamma^{\text{ss}}(\mathbf{x}) \end{pmatrix}$ is the coefficients matrix at point \mathbf{x} , and $\gamma^{\text{pp}}, \gamma^{\text{ps}}, \gamma^{\text{sp}}, \gamma^{\text{ss}}$ are the subsurface reflector coefficients corresponding to different wave types and $\mathbf{y}_k = \int s_k(t) * \mathbf{y}(\mathbf{x}) dS(\mathbf{x})$ and $*$ stands for convolution.

Elastic envelope inversion using multicomponent seismic data without low frequency

C. Huang et al.

Title Page

Abstract

Introduction

Conclusions

References

Tables

Figures

◀

▶

◀

▶

Back

Close

Full Screen / Esc

Printer-friendly Version

Interactive Discussion



Elastic envelope inversion using multicomponent seismic data without low frequency

C. Huang et al.

Title Page

Abstract

Introduction

Conclusions

References

Tables

Figures

◀

▶

◀

▶

Back

Close

Full Screen / Esc

Printer-friendly Version

Interactive Discussion

$$\mathbf{G}_{ik}^{sr}(t; \mathbf{x}_r, \mathbf{x}_s) = \mathbf{G}_{jk}^T(t, \mathbf{x}; \mathbf{x}_s) * \mathbf{G}_{ij}(t, \mathbf{x}_r; \mathbf{x}), \quad \mathbf{G}_{jk}(t, \mathbf{x}; \mathbf{x}_s) = \begin{pmatrix} G_{jk}^P(t, \mathbf{x}; \mathbf{x}_s) \\ G_{jk}^S(t, \mathbf{x}; \mathbf{x}_s) \end{pmatrix},$$

$\mathbf{G}_{ij}(t, \mathbf{x}_r; \mathbf{x}) = \begin{pmatrix} G_{ij}^P(t, \mathbf{x}_r; \mathbf{x}) \\ G_{ij}^S(t, \mathbf{x}_r; \mathbf{x}) \end{pmatrix}$ and $G_{ik}^P, G_{ik}^S, G_{kj}^P, G_{kj}^S$ are P-wave and S-wave forward modeling Green functions.

From Eq. (10), we see clearly where the low frequency in envelope comes from.

For the first term in the right side of Eq. (10), the envelope of high-frequency original wavelet is low-resolution (shown in Fig. 1); for the second term, because $\boldsymbol{\gamma}(\mathbf{x})$ is assumed to be random series, the spectrum of $\boldsymbol{\gamma}_k(t)$ is determined by wavelet. Hence, low frequency information containing in signal $\boldsymbol{\gamma}_k$ is extracted by envelope operator $E^2(\boldsymbol{\gamma}_k(t))$. Additionally, the low frequency information containing in \mathbf{G}_{ik}^{sr} remains unchanged and is beneficial to recover the background velocity models.

In the process of EFWI, the inversion shall firstly recover the structure corresponding to the frequencies whose energy are the largest in the data. Therefore, due to the strong low frequency contained in envelope, the elastic envelope inversion shall firstly recover the long-wavelength of the subsurface model, which behaves as the first step of multiscale strategy. That is why we can use results produced by envelope elastic inversion as the starting model for conventional EFWI. According to the advantage of elastic envelope inversion, we present a two-step elastic inversion strategy. In the first step, elastic envelope inversion is used to recover the low-wavenumber components of the subsurface model. Then, the obtained results in first step are used as the starting models for conventional EFWI to recover high-wavenumber components. And some numerical examples are presented in the next section to prove the effectiveness of the two-step elastic inversion strategy.

3 Numerical tests

We test our two-step elastic envelope inversion strategy on a modified 2-D elastic Marmousi-2 model (Martin et al., 2002). In order to reduce the computation burden, we remove the upper water layer and keep only the central portion of the P-wave velocity model from the original Marmousi-2 model. Then the S-wave velocity model is regenerated from the original P-wave velocity model using formula (11). In this formula, we use two V_s/V_p ratios and the nonlinearity of the inversion is surely increased comparing with that only uses one V_s/V_p ratio.

$$V_s = \begin{cases} 0.6V_p & V_p < 3.5 \text{ km s}^{-1} \\ \frac{1}{\sqrt{3}}V_p & V_p \geq 3.5 \text{ km s}^{-1} \end{cases} \quad (11)$$

During the inversion, we keep density constant and assumed to be known as 2.3 g cm^{-3} . Figure 13 shows the modified Marmousi-2 V_p and V_s models. Elastic wave simulation is performed with a high-order staggered grid finite-difference method in time domain. The dimension of the model is $10.0 \text{ km} \times 3.1 \text{ km}$ and the grid interval is 12.5 m in horizontal and 25 m in vertical.

To reduce the nonlinearity of the inversion caused by free-surface effects (Brossier et al., 2009), an absorbing boundary is placed on the top of the models. To simulate on-shore synthetic data on the Marmousi-2 model, 80 explosive sources along the surface are inspired with the interval of 125 m . A Ricker wavelet with the dominant frequency of 8 Hz is used as the source function. Here we apply a roll in/out survey system. For every shot, 401 two component receivers are spaced every 12.5 m along the top surface and the source is in the center of the receiver line. 1-D constant gradient models (Fig. 14) are taken as the starting models in our tests. Two types of seismic data are used in inversion: one is the original synthetic data and the other is the synthetic data by filtering out frequency below 5 Hz . To each type of data, both conventional EFWI and our two-step inversion are applied.

Elastic envelope inversion using multicomponent seismic data without low frequency

C. Huang et al.

Title Page

Abstract

Introduction

Conclusions

References

Tables

Figures

◀

▶

◀

▶

Back

Close

Full Screen / Esc

Printer-friendly Version

Interactive Discussion



Elastic envelope inversion using multicomponent seismic data without low frequency

C. Huang et al.

Title Page

Abstract

Introduction

Conclusions

References

Tables

Figures

◀

▶

◀

▶

Back

Close

Full Screen / Esc

Printer-friendly Version

Interactive Discussion

In the first type of test, we use the synthetic 2C data as input to do both conventional EFWI and elastic envelope inversion. Figure 15 shows the revealed results of conventional EFWI after 100 iterations. Because the gradient starting models deviate substantially from the true models and strong ultra-low frequency is unavailable in the data (as shown in Fig. 4), conventional EFWI suffers from cycle-skipping problem and fails to converge to acceptable results. During this inversion, only short wavelength components are updated while at incorrect positions. The inversion process itself is unstable.

Figure 16 shows the results of the elastic envelope inversion. From the results, we can see that the long-wavelength components of the subsurface models are well recovered. Then, we put the results as the starting models for conventional EFWI in the second step and the final results are shown in Fig. 17. We can obviously see that, after the second step inversion, the short wavelength components of the subsurface models are updated at the right positions and high resolution results are finally achieved. Comparing results in Fig. 15 with Fig. 17, final results of two-step inversion are much better than conventional EFWI. The improvements are more obvious on the vertical profiles (V_p and V_s vertical slices at position of 2, 5 and 8 km in Figs. 18–20). Additionally, the improvements on V_s are more obvious than V_p .

In the second test, inversions are implemented with the filtered synthetic data whose frequencies below 5 Hz are filtered out. We can see that the results of the conventional EFWI (Fig. 21) are even worse than those in Fig. 15, especially for V_s . Meanwhile, the inversion process becomes more unstable. However, after the first step of the proposed inversion strategy, smooth background models can be produced (Fig. 22) and they are similar to those obtained in the first test shown in Fig. 16. This emphasizes the fact that the elastic envelope inversion has the ability to recover the background model even with poor starting models and without low frequency in seismic records. Using results shown in Fig. 22 as the starting model for the conventional EFWI, we can obtain acceptable final results (Fig. 23) which is also similar to those (shown in Fig. 17) in the first test. The vertical profiles (shown in Figs. 24–26) extracted from final results at the locations

of 2, 5 and 8 km further prove the superiority of our two-step inversion strategy. More improvements in V_s result again show the effectiveness of our elastic envelope inversion for updating S-wave velocity.

4 Conclusion

Envelope operator can demodulate the multicomponent data and extract strong low frequency modulation signal contained in recorded data. After envelope transform, most energy of the corresponding envelope are concentrated on ultra-low frequencies zone. With the benefit of these strong ultra-low frequency information, the long-wavelength components of the subsurface model can be well recovered by elastic envelope inversion. It behaves as a natural multi-scale strategy which starts from the ultra-low frequency. Hence, the nonlinearity and the starting-model dependence of elastic envelope inversion are greatly reduced. The elastic envelope inversion is an effective and robust method to achieve accurate background model using the collected multicomponent data, even when the low frequency information is missing in the data.

Appendix A:

Elastic multicomponent displacement for a point source can be represented in frequency domain as

$$u_i(\omega, \mathbf{x}; \mathbf{x}_s) = G_{ik}(\omega, \mathbf{x}; \mathbf{x}_s) s_k(\omega), \quad (\text{A1})$$

where $\mathbf{u}(u_i(\omega, \mathbf{x}; \mathbf{x}_s), i = x, y, z)$ is the displacement, $\mathbf{s}(\omega) \{s_k(\omega), k = x, y, z\}$ is the wavelet function applied at position \mathbf{x}_s and G_{ik} is the elastic dynamic Green's function which can be decomposed into two parts: one for P-wave and the other for S-wave,

$$G_{ik}(\omega, \mathbf{x}; \mathbf{x}_s) = G_{ik}^P(\omega, \mathbf{x}; \mathbf{x}_s) + G_{ik}^S(\omega, \mathbf{x}; \mathbf{x}_s). \quad (\text{A2})$$

Elastic envelope inversion using multicomponent seismic data without low frequency

C. Huang et al.

Title Page

Abstract

Introduction

Conclusions

References

Tables

Figures

◀

▶

◀

▶

Back

Close

Full Screen / Esc

Printer-friendly Version

Interactive Discussion



Multicomponent records can be decomposed as

$$u_i(\omega, \mathbf{x}_r; \mathbf{x}_s) = u_i^f(\omega, \mathbf{x}_r; \mathbf{x}_s) + u_i^{sc}(\omega, \mathbf{x}_r; \mathbf{x}_s), \quad (\text{A3})$$

where $\mathbf{u}^f \{u_i^f(\omega, \mathbf{x}_r; \mathbf{x}_s), i = x, y, z\}$ is the direct wavefield in the background medium and $\mathbf{u}^{sc} \{u_i^{sc}(\omega, \mathbf{x}_r; \mathbf{x}_s), i = x, y, z\}$ is the backscattered wavefield at \mathbf{x}_r due to a source at \mathbf{x}_s .

5 Ignoring the multiples, the backscattered wavefield can be expressed as

$$u_i^{sc}(\omega, \mathbf{x}_r; \mathbf{x}_s) = s_k(\omega) \int G_{jk}(\omega, \mathbf{x}; \mathbf{x}_s) R(\mathbf{x}) G_{ij}(\omega, \mathbf{x}_r; \mathbf{x}) dS(\mathbf{x}). \quad (\text{A4})$$

$R(\mathbf{x})$ is a response function that measures the strength of the reflected response. If we put Eq. (A2) into Eq. (A4) and replace $R(\mathbf{x})$ with reflection coefficients $\boldsymbol{\gamma}(\mathbf{x})$, we get

$$\begin{aligned} u_i^{sc}(t, \mathbf{x}_r; \mathbf{x}_s) &= s_k(\omega) \int \begin{pmatrix} G_{jk}^P(\omega, \mathbf{x}; \mathbf{x}_s) G_{ij}^P(\omega, \mathbf{x}_r; \mathbf{x}) \boldsymbol{\gamma}^{PP}(\mathbf{x}) \\ + G_{jk}^S(\omega, \mathbf{x}; \mathbf{x}_s) G_{ij}^P(\omega, \mathbf{x}_r; \mathbf{x}) \boldsymbol{\gamma}^{SP}(\mathbf{x}) \\ + G_{jk}^P(\omega, \mathbf{x}; \mathbf{x}_s) G_{ij}^S(\omega, \mathbf{x}_r; \mathbf{x}) \boldsymbol{\gamma}^{PS}(\mathbf{x}) \\ + G_{jk}^S(\omega, \mathbf{x}; \mathbf{x}_s) G_{ij}^S(\omega, \mathbf{x}_r; \mathbf{x}) \boldsymbol{\gamma}^{SS}(\mathbf{x}) \end{pmatrix} dS(\mathbf{x}) \quad (\text{A5}) \\ &= s_k(\omega) \int \begin{pmatrix} G_{jk}^P(\omega, \mathbf{x}; \mathbf{x}_s) \\ G_{jk}^S(\omega, \mathbf{x}; \mathbf{x}_s) \end{pmatrix}^T \begin{pmatrix} \boldsymbol{\gamma}^{PP}(\mathbf{x}) & \boldsymbol{\gamma}^{PS}(\mathbf{x}) \\ \boldsymbol{\gamma}^{SP}(\mathbf{x}) & \boldsymbol{\gamma}^{SS}(\mathbf{x}) \end{pmatrix} \begin{pmatrix} G_{ij}^P(\omega, \mathbf{x}_r; \mathbf{x}) \\ G_{ij}^S(\omega, \mathbf{x}_r; \mathbf{x}) \end{pmatrix} dS(\mathbf{x}) \\ &= s_k(\omega) \int \mathbf{G}_{jk}^T(\omega, \mathbf{x}; \mathbf{x}_s) \boldsymbol{\gamma}(\mathbf{x}) \mathbf{G}_{ij}(\omega, \mathbf{x}_r; \mathbf{x}) dS(\mathbf{x}), \end{aligned}$$

10 where $\mathbf{G}_{jk}(\omega, \mathbf{x}; \mathbf{x}_s) = \begin{pmatrix} G_{jk}^P(\omega, \mathbf{x}; \mathbf{x}_s) \\ G_{jk}^S(\omega, \mathbf{x}; \mathbf{x}_s) \end{pmatrix}$, $\mathbf{G}_{ij}(\omega, \mathbf{x}_r; \mathbf{x}) = \begin{pmatrix} G_{ij}^P(\omega, \mathbf{x}_r; \mathbf{x}) \\ G_{ij}^S(\omega, \mathbf{x}_r; \mathbf{x}) \end{pmatrix}$, and $\boldsymbol{\gamma}(\mathbf{x}) =$

$\begin{pmatrix} \boldsymbol{\gamma}^{PP}(\mathbf{x}) & \boldsymbol{\gamma}^{SP}(\mathbf{x}) \\ \boldsymbol{\gamma}^{PS}(\mathbf{x}) & \boldsymbol{\gamma}^{SS}(\mathbf{x}) \end{pmatrix}$ is the coefficients matrix at point \mathbf{x} , and $\boldsymbol{\gamma}^{PP}, \boldsymbol{\gamma}^{PS}, \boldsymbol{\gamma}^{SP}, \boldsymbol{\gamma}^{SS}$ are the sub-surface reflector coefficients corresponding to different wave types. $S(\mathbf{x})$ stands for all

the reflection surfaces in the model. $G_{ik}^P, G_{ik}^S, G_{kj}^P, G_{kj}^S$ are P-wave and S-wave forward modeling Green functions.

Equation (A5) can be rewritten in time domain as

$$u_i^{SC}(t, \mathbf{x}_r; \mathbf{x}_s) = s_k(t) * \int \mathbf{G}_{ik}^{SR}(t; \mathbf{x}_r, \mathbf{x}_s) \boldsymbol{\gamma}(\mathbf{x}) dS(\mathbf{x}), \quad (\text{A6})$$

- 5 where the function $\mathbf{G}_{ik}^{SR}(t; \mathbf{x}_r, \mathbf{x}_s) = \mathbf{G}_{jk}^T(t, \mathbf{x}; \mathbf{x}_s) * \mathbf{G}_{ij}(t, \mathbf{x}_r; \mathbf{x})$ only modifies the travel time and amplitude of the reflection events. According to Wu et al. (2014), the propagator \mathbf{G}_{ik}^{SR} is a smoothly varying function and can be separated from convolution operator. Hence, we can approximate Eq. (A6) as

$$\begin{aligned} u_i^{SC}(t, \mathbf{x}_r; \mathbf{x}_s) &\cong \mathbf{G}_{ik}^{SR}(t; \mathbf{x}_r, \mathbf{x}_s) \int s_k(t) * \boldsymbol{\gamma}(\mathbf{x}) dS(\mathbf{x}), \\ &= \mathbf{G}_{ik}^{SR}(t; \mathbf{x}_r, \mathbf{x}_s) \boldsymbol{\gamma}_k, \end{aligned} \quad (\text{A7})$$

- 10 where $\boldsymbol{\gamma}_k = \int s_k(t) * \boldsymbol{\gamma}(\mathbf{x}) dS(\mathbf{x})$. In modulation theory, we can treat $\boldsymbol{\gamma}_k$ as the carrier signal and \mathbf{G}_{ik}^{SR} as the modulated signal. Because \mathbf{G}_{ik}^{SR} is smooth, the spectrum of the modulated signal is mainly determined by the source wavelet. Similarly, the direct wave can be expressed as

$$u_i^f(t, \mathbf{x}_r; \mathbf{x}_s) = s_k(t) * G_{ik}^f(t; \mathbf{x}_r, \mathbf{x}_s), \quad (\text{A8})$$

- 15 where G_{ik}^f is the Green's function for the direct arrival. In Born theory, G_{ik}^f is assumed to be a much slower time-varying function than the source wavelet. And the direct arrivals is single or sparse, thus we can approximate the convolution by multiple. Then we get

$$u_i^f(t, \mathbf{x}_r; \mathbf{x}_s) = G_{ik}^f(t; \mathbf{x}_r, \mathbf{x}_s) s_k(t). \quad (\text{A9})$$

Inserting Eqs. (A9) and (A7) into Eq. (A3), we have

$$20 \quad u_i(t, \mathbf{x}_r; \mathbf{x}_s) = G_{ik}^f(t; \mathbf{x}_r, \mathbf{x}_s) s_k(t) + \mathbf{G}_{ik}^{SR}(t; \mathbf{x}_r, \mathbf{x}_s) \boldsymbol{\gamma}_k(t). \quad (\text{A10})$$

Elastic envelope inversion using multicomponent seismic data without low frequency

C. Huang et al.

Title Page

Abstract

Introduction

Conclusions

References

Tables

Figures

◀

▶

◀

▶

Back

Close

Full Screen / Esc

Printer-friendly Version

Interactive Discussion



We can treat Eq. (A10) as a product of two functions: a carrier signal and a modulation signal. For the first term on the right side, the carrier signal is the source wavelet and the modulator is the direct propagator; for the second term, the carrier is $\boldsymbol{\gamma}_k$ and the modulator is \mathbf{G}_{ik}^{sr} . \mathbf{G}_{ik}^{sr} and G_{ik}^f are smooth and surely contain low frequency, but after modulation, the spectrum of signal u_i is mainly determined by the spectrum of wavelet. However, if we apply Hilbert transform to Eq. (A10)

$$H\{u_i(t, \mathbf{x}_r; \mathbf{x}_s)\} = H\left\{G_{ik}^f(t; \mathbf{x}_r, \mathbf{x}_s)s_k(t) + \mathbf{G}_{ik}^{sr}(t; \mathbf{x}_r, \mathbf{x}_s)\boldsymbol{\gamma}_k(t)\right\}. \quad (\text{A11})$$

Then \mathbf{G}_{ik}^{sr} and G_{ik}^f can be pulled out from the transformation. Thus we can rewrite Eq. (A11) as

$$H\{u_i(t, \mathbf{x}_r; \mathbf{x}_s)\} = G_{ik}^f(t; \mathbf{x}_r, \mathbf{x}_s)H\{s_k(t)\} + \mathbf{G}_{ik}^{sr}(t; \mathbf{x}_r, \mathbf{x}_s)H\{\boldsymbol{\gamma}_k(t)\}. \quad (\text{A12})$$

The envelope function can be expressed by

$$E^2(u_i(t)) = u_i^2(t) + \{H(u_i(t))\}^2. \quad (\text{A13})$$

Inserting Eq. (A12) to Eq. (A13), and neglecting the crosstalk between the first and the second term in Eq. (A11), we get

$$\begin{aligned} E^2(u_i(t)) &\approx \left(G_{ik}^f(t)\right)^2 \left[\left(s_k(t)\right)^2 + \{H[s_k(t)]\}^2\right] + \left(\mathbf{G}_{ik}^{sr}(t)\right)^2 \left[\left(\boldsymbol{\gamma}_k(t)\right)^2 + \{H[\boldsymbol{\gamma}_k(t)]\}^2\right] \\ &= \left(G_{ik}^f(t)\right)^2 E^2(s_k(t)) + \left(\mathbf{G}_{ik}^{sr}(t)\right)^2 E^2(\boldsymbol{\gamma}_k(t)) \end{aligned} \quad (\text{A14})$$

Acknowledgements. The authors gratefully acknowledge the financial supports by the National Science and Technology Major Project of China (Grant No. 2011ZX05005-005-007HZ) and the National Natural Science Foundation of China (Grant No. 41274116, 41474034).

References

- Baeten, G., de Maag, J. W., Plessix, R. E., Klaassen, R., Qureshi, T., Kleemeyer, M., ten Kroode, F., and Rujie, Z.: The use of low frequencies in a full-waveform inversion and impedance inversion land seismic case study, *Geophys. Prospect.*, 61, 701–711, 2013.
- 5 Bozdağ, E., Trampert, J., and Tromp, J.: Misfit functions for full waveform inversion based on instantaneous phase and envelope measurements, *Geophys. J. Int.*, 185, 845–870, 2011.
- Brenders, A. J. and Pratt, R. G.: Full waveform tomography for lithospheric imaging: results from a blind test in a realistic crustal model, *Geophys. J. Int.*, 168, 133–151, 2007.
- 10 Brossier, R., Operto, S., and Virieux, J.: Seismic imaging of complex onshore structures by 2D elastic frequency-domain full-waveform inversion, *Geophysics*, 74, WCC105–WCC118, 2009.
- Bunks, C., Saleck, F. M., Zaleski, S., and Chavent, G.: Multiscale seismic waveform inversion, *Geophysics*, 60, 1457–1473, 1995.
- Nonlinear least squares for inverse problems: theoretical foundations and step-by-step guide for applications, Springer, New York, 2009.
- 15 Chi, B., Dong, L., and Liu, Y.: Full waveform inversion method using envelope objective function without low frequency data, *J. Appl. Geophys.*, 109, 36–46, 2014.
- Fichtner, A. and Trampert, J.: Resolution analysis in full waveform inversion, *Geophys. J. Int.*, 187, 1604–1624, 2011.
- 20 Gauthier, O., Virieux, J., and Tarantola, A.: Two-dimensional nonlinear inversion of seismic waveforms: numerical results, *Geophysics*, 51, 1387–1403, 1986.
- Gholami, Y., Brossier, R., Operto, S., Ribodetti, A., and Virieux, J.: Which parameterization is suitable for acoustic vertical transverse isotropic full waveform inversion? Part 1: Sensitivity and trade-off analysis, *Geophysics*, 78, R81–R105, 2013.
- 25 Liu, Q. and Tromp, J.: Finite-frequency kernels based on adjoint methods, *B. Seismol. Soc. Am.*, 96, 2383–2397, 2006.
- Luo, Y. and Schuster, G. T.: Wave-equation travelttime inversion, *Geophysics*, 56, 645–653, 1991.
- 30 Martin, G. S., Larsen, S., and Marfurt, K.: Marmousi-2: an updated model for the investigation of AVO in structurally complex areas, 2002 SEG Annual Meeting, 6–11 October, Salt Lake City, Utah, Expanded Abstracts, 1979–1982, 2002.

Elastic envelope inversion using multicomponent seismic data without low frequency

C. Huang et al.

Title Page

Abstract

Introduction

Conclusions

References

Tables

Figures

◀

▶

◀

▶

Back

Close

Full Screen / Esc

Printer-friendly Version

Interactive Discussion



Elastic envelope inversion using multicomponent seismic data without low frequency

C. Huang et al.

[Title Page](#)

[Abstract](#)

[Introduction](#)

[Conclusions](#)

[References](#)

[Tables](#)

[Figures](#)

[⏪](#)

[⏩](#)

[◀](#)

[▶](#)

[Back](#)

[Close](#)

[Full Screen / Esc](#)

[Printer-friendly Version](#)

[Interactive Discussion](#)



Mora, P.: Nonlinear two-dimensional elastic inversion of multioffset seismic data, *Geophysics*, 52, 1211–1228, 1987.

Pratt, R. G., Song, Z. M., Williamson, P., and Warner, M.: Two-dimensional velocity models from wide-angle seismic data by wavefield inversion, *Geophys. J. Int.*, 124, 323–340, 1996.

5 Pratt, R. G., Shin, C., and Hick, G. J.: Gauss–Newton and full Newton methods in frequency–space seismic waveform inversion, *Geophys. J. Int.*, 133, 341–362, 1998.

Plessix, R.-E.: A review of the adjoint-state method for computing the gradient of a functional with geophysical applications, *Geophys. J. Int.*, 167, 495–503, 2006.

10 Plessix, R. É. and Cao, Q.: A parametrization study for surface seismic full waveform inversion in an acoustic vertical transversely isotropic medium, *Geophys. J. Int.*, 185, 539–556, 2011.

Shin, C. and Cha, Y. H.: Waveform inversion in the Laplace domain, *Geophys. J. Int.*, 173, 922–931, 2008.

Sirgue, L. and Pratt, R. G.: Efficient waveform inversion and imaging: a strategy for selecting temporal frequencies, *Geophysics*, 69, 231–248, 2004.

15 Tarantola, A.: Inversion of seismic reflection data in the acoustic approximation, *Geophysics*, 49, 1259–1266, 1984.

Tatham, R. H. and Stoffa, P. L.: V_p/V_s – a potential hydrocarbon indicator, *Geophysics*, 41, 837–849, 1976.

20 Virieux, J. and Operto, S.: An overview of full-waveform inversion in exploration geophysics, *Geophysics*, 74, WCC1–WCC26, 2009.

Wu, R. S., Luo, J., and Wu, B.: Seismic envelope inversion and modulation signal model, *Geophysics*, 79, WA13–WA24, 2014.

Zhang, S., Schuster, G., and Luo, Y.: Wave-equation Reflection Traveltime Inversion. 2011 SEG Annual Meeting, 18–23 September, San Antonio, Texas, Expanded Abstracts, 2705–2709,

25 2011.

Elastic envelope inversion using multicomponent seismic data without low frequency

C. Huang et al.

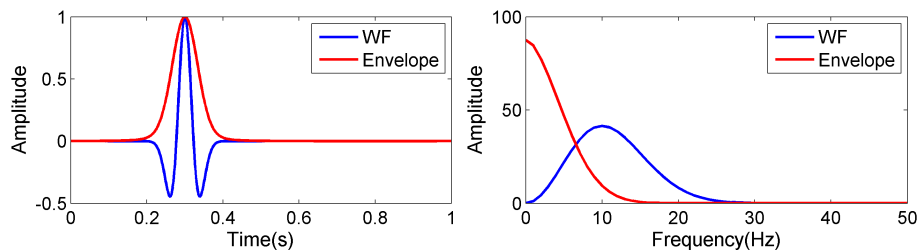


Figure 1. Left: Ricker wavelet (blue line) and its envelope (red line); right: the corresponding spectra of the Ricker wavelet (blue line) and its corresponding envelope (red line).

[Title Page](#)[Abstract](#)[Introduction](#)[Conclusions](#)[References](#)[Tables](#)[Figures](#)[◀](#)[▶](#)[◀](#)[▶](#)[Back](#)[Close](#)[Full Screen / Esc](#)[Printer-friendly Version](#)[Interactive Discussion](#)

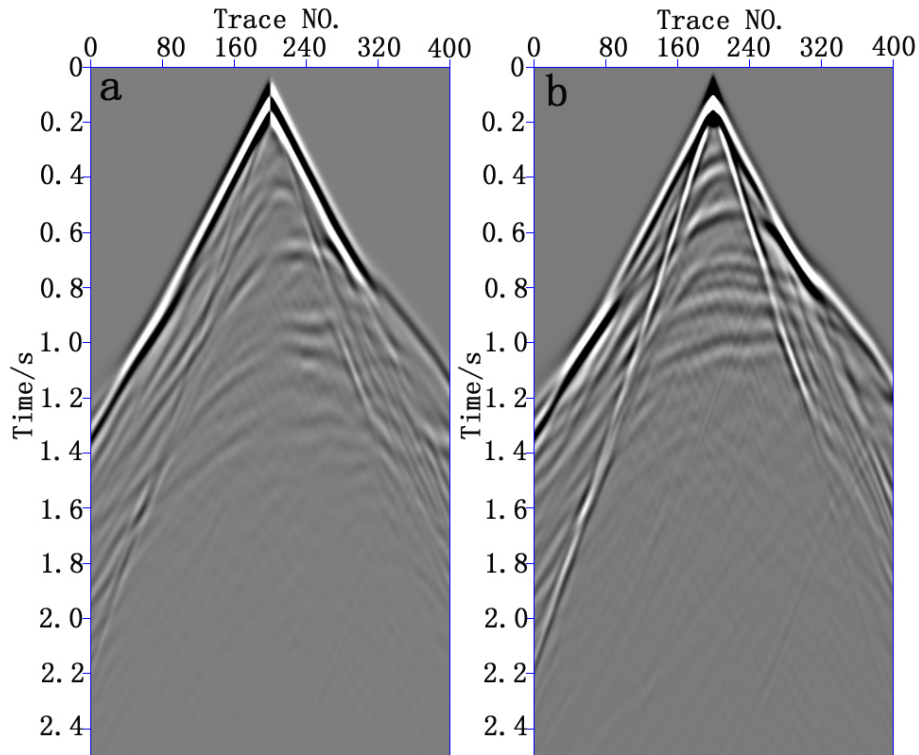


Figure 2. Seismograms computed in the modified Marmousi-2 model for **(a)** horizontal and **(b)** vertical components of the particle displacement.

Elastic envelope inversion using multicomponent seismic data without low frequency

C. Huang et al.

Title Page	
Abstract	Introduction
Conclusions	References
Tables	Figures
◀	▶
◀	▶
Back	Close
Full Screen / Esc	
Printer-friendly Version	
Interactive Discussion	



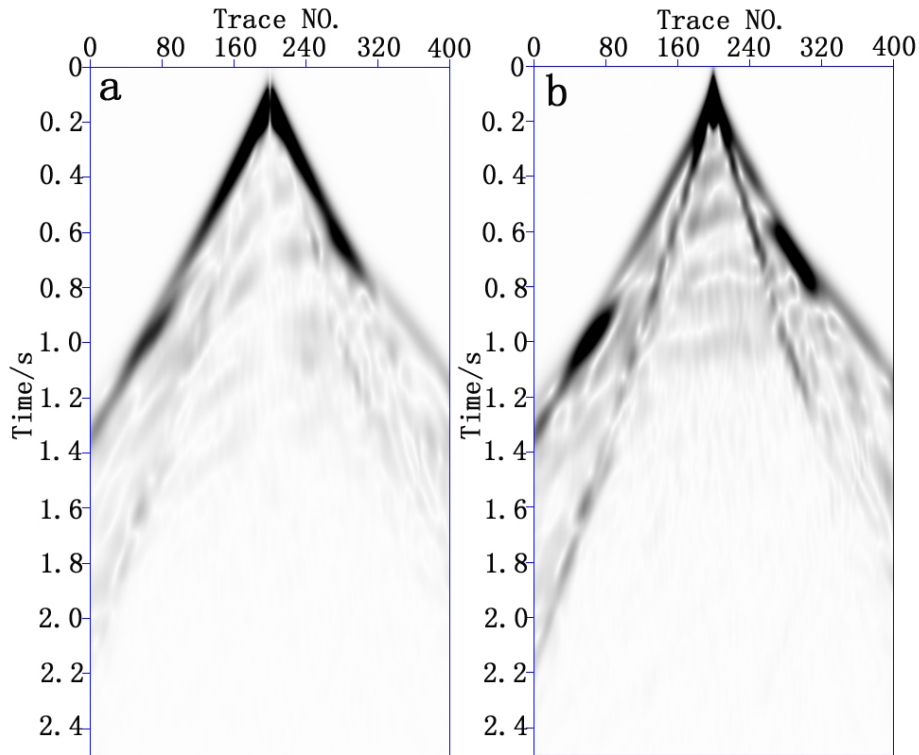


Figure 3. The corresponding envelopes of shot profiles in Fig. 2 (**a** horizontal component; **b** vertical component).

Elastic envelope inversion using multicomponent seismic data without low frequency

C. Huang et al.

Title Page	
Abstract	Introduction
Conclusions	References
Tables	Figures
◀	▶
◀	▶
Back	Close
Full Screen / Esc	
Printer-friendly Version	
Interactive Discussion	



Elastic envelope inversion using multicomponent seismic data without low frequency

C. Huang et al.

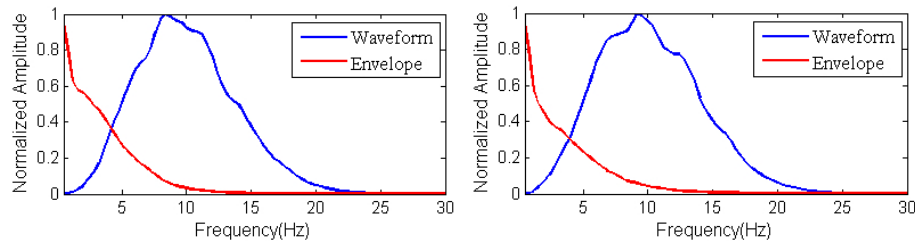


Figure 4. Spectra of the horizontal (left) and vertical (right) components of the seismograms (Fig. 2) and the corresponding envelope (Fig. 3).

[Title Page](#)[Abstract](#)[Introduction](#)[Conclusions](#)[References](#)[Tables](#)[Figures](#)[◀](#)[▶](#)[◀](#)[▶](#)[Back](#)[Close](#)[Full Screen / Esc](#)[Printer-friendly Version](#)[Interactive Discussion](#)

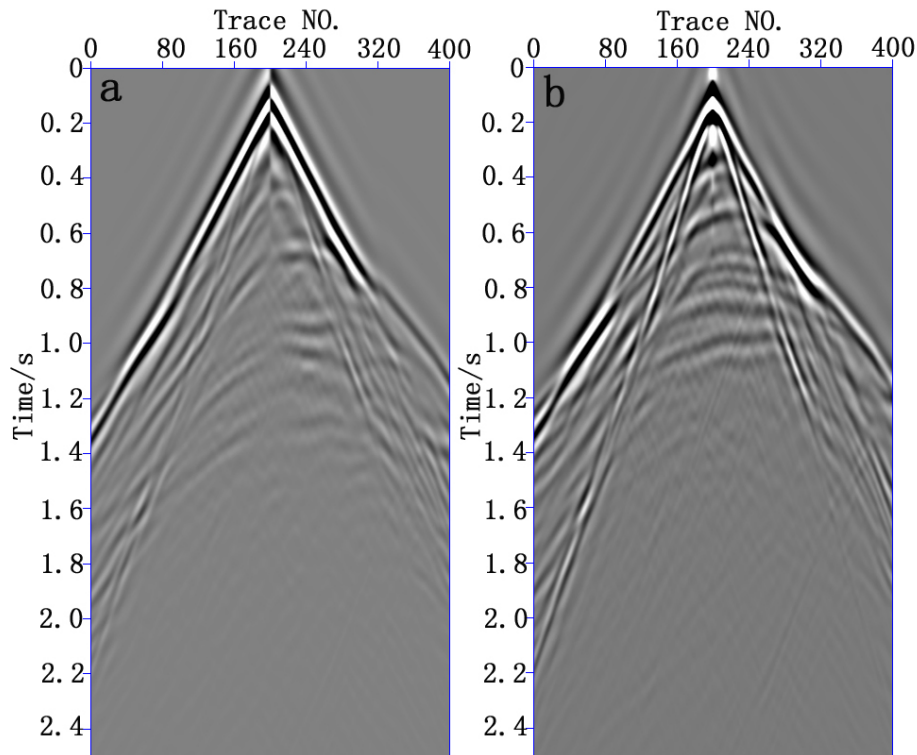


Figure 5. Seismograms computed in the modified Marmousi-2 model for **(a)** horizontal and **(b)** vertical components of the particle displacement after high-pass filtering.

Elastic envelope inversion using multicomponent seismic data without low frequency

C. Huang et al.

Title Page	
Abstract	Introduction
Conclusions	References
Tables	Figures
◀	▶
◀	▶
Back	Close
Full Screen / Esc	
Printer-friendly Version	
Interactive Discussion	



Elastic envelope inversion using multicomponent seismic data without low frequency

C. Huang et al.

Title Page

Abstract

Introduction

Conclusions

References

Tables

Figures

◀

▶

◀

▶

Back

Close

Full Screen / Esc

Printer-friendly Version

Interactive Discussion

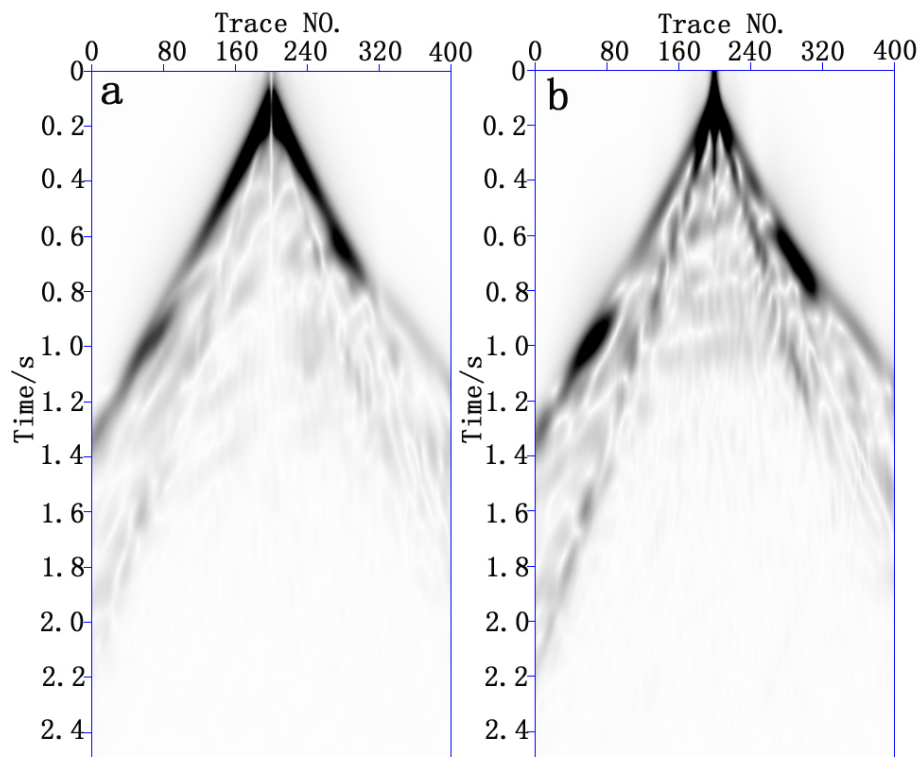


Figure 6. The corresponding envelope of shot profiles in Fig. 5 (**a** horizontal component; **b** vertical component).

Elastic envelope inversion using multicomponent seismic data without low frequency

C. Huang et al.

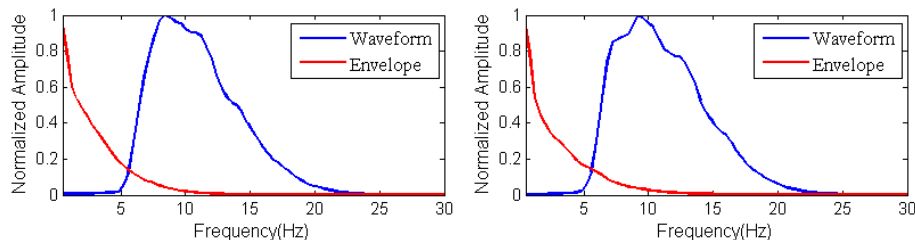


Figure 7. The spectra of the horizontal (left) and vertical (right) components of the seismograms (Fig. 5) and the corresponding envelope (Fig. 6).

[Title Page](#)[Abstract](#)[Introduction](#)[Conclusions](#)[References](#)[Tables](#)[Figures](#)[⏪](#)[⏩](#)[◀](#)[▶](#)[Back](#)[Close](#)[Full Screen / Esc](#)[Printer-friendly Version](#)[Interactive Discussion](#)

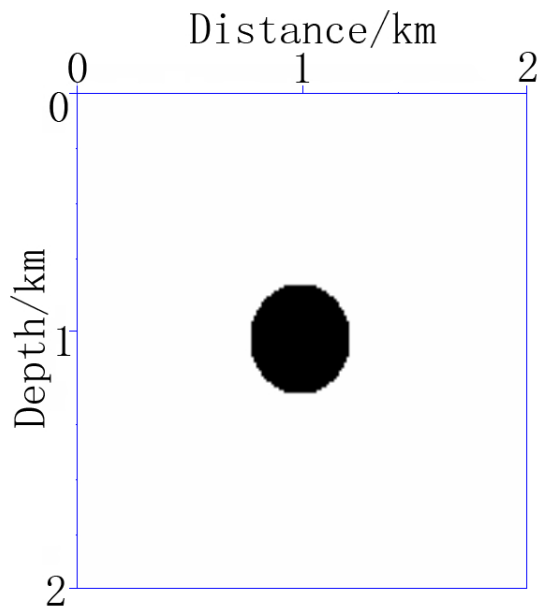


Figure 8. Simple inclusion model.

Elastic envelope inversion using multicomponent seismic data without low frequency

C. Huang et al.

Title Page

Abstract

Introduction

Conclusions

References

Tables

Figures

◀

▶

◀

▶

Back

Close

Full Screen / Esc

Printer-friendly Version

Interactive Discussion



Elastic envelope inversion using multicomponent seismic data without low frequency

C. Huang et al.

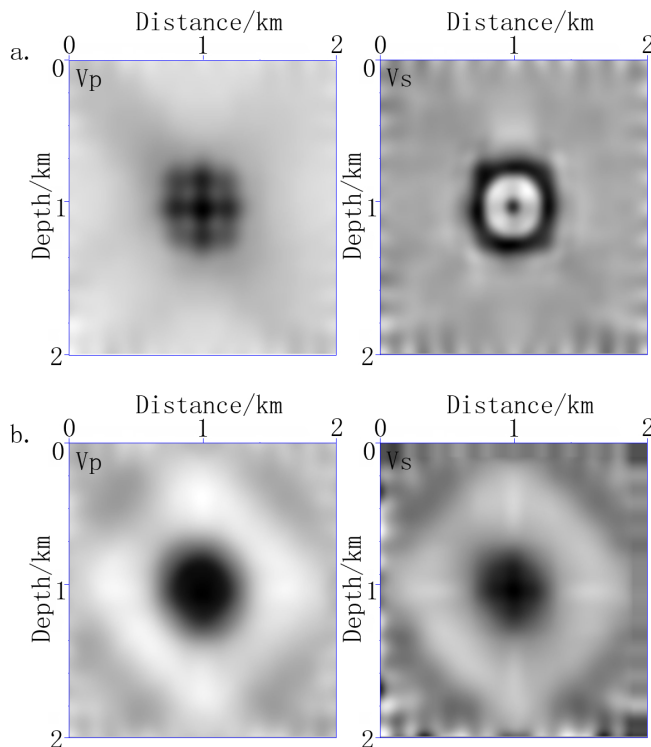


Figure 9. Gradient of V_p and V_s in the first iteration of inversion (**a** conventional EFWI; **b** elastic envelope inversion).

Elastic envelope inversion using multicomponent seismic data without low frequency

C. Huang et al.

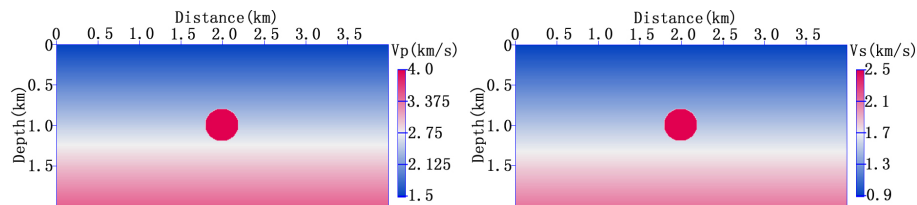


Figure 10. Inclusion velocity models.

Title Page

Abstract

Introduction

Conclusions

References

Tables

Figures

◀

▶

◀

▶

Back

Close

Full Screen / Esc

Printer-friendly Version

Interactive Discussion

Elastic envelope inversion using multicomponent seismic data without low frequency

C. Huang et al.

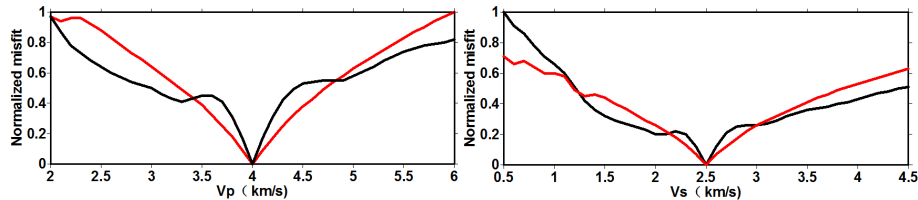


Figure 11. Objective functions for the conventional EFWI (black line) and elastic envelope inversion (red line) with respect to V_p and V_s variations.

[Title Page](#)[Abstract](#)[Introduction](#)[Conclusions](#)[References](#)[Tables](#)[Figures](#)[◀](#)[▶](#)[◀](#)[▶](#)[Back](#)[Close](#)[Full Screen / Esc](#)[Printer-friendly Version](#)[Interactive Discussion](#)

Elastic envelope inversion using multicomponent seismic data without low frequency

C. Huang et al.

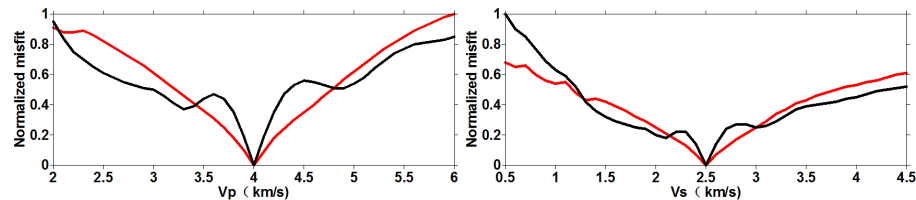


Figure 12. Objective functions for the conventional EFWI (black line) and elastic envelope inversion (red line) with respect to V_p and V_s variations using filtered data.

Title Page

Abstract

Introduction

Conclusions

References

Tables

Figures

◀

▶

◀

▶

Back

Close

Full Screen / Esc

Printer-friendly Version

Interactive Discussion



Elastic envelope inversion using multicomponent seismic data without low frequency

C. Huang et al.

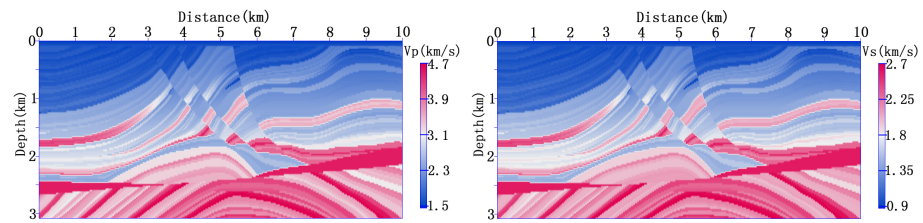


Figure 13. 2-D Elastic Marmousi-2 models.

Title Page	
Abstract	Introduction
Conclusions	References
Tables	Figures
◀	▶
◀	▶
Back	Close
Full Screen / Esc	
Printer-friendly Version	
Interactive Discussion	



Elastic envelope inversion using multicomponent seismic data without low frequency

C. Huang et al.

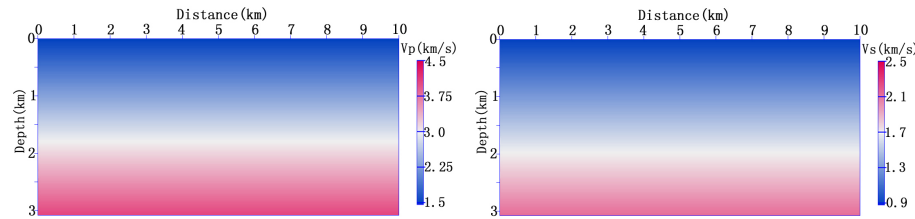
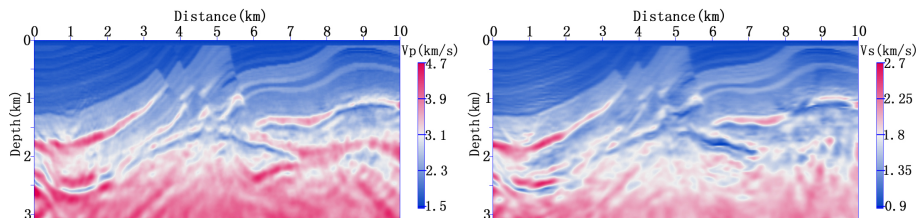


Figure 14. Linear gradient starting models.

Title Page	
Abstract	Introduction
Conclusions	References
Tables	Figures
◀	▶
◀	▶
Back	Close
Full Screen / Esc	
Printer-friendly Version	
Interactive Discussion	

Elastic envelope inversion using multicomponent seismic data without low frequency

C. Huang et al.

**Figure 16.** Results obtained by elastic envelope inversion in the first test.[Title Page](#)[Abstract](#)[Introduction](#)[Conclusions](#)[References](#)[Tables](#)[Figures](#)[◀](#)[▶](#)[◀](#)[▶](#)[Back](#)[Close](#)[Full Screen / Esc](#)[Printer-friendly Version](#)[Interactive Discussion](#)

Elastic envelope inversion using multicomponent seismic data without low frequency

C. Huang et al.

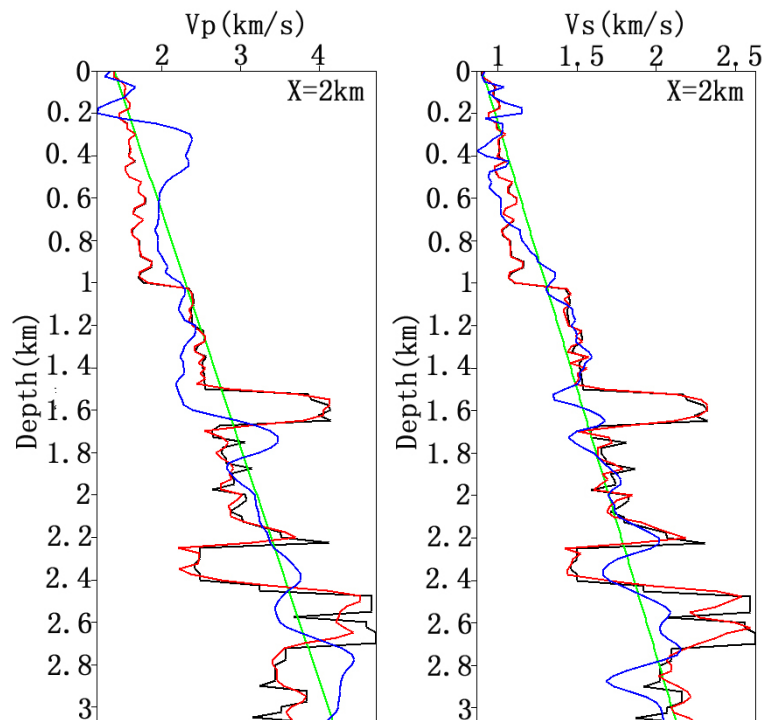


Figure 18. Comparison between velocity profiles extracted from models recovered by conventional EFWI (blue line) and our method (red line) for V_p and V_s in the first test at the location of 2 km. Starting and true models are depicted with green and black lines, respectively.

Elastic envelope inversion using multicomponent seismic data without low frequency

C. Huang et al.

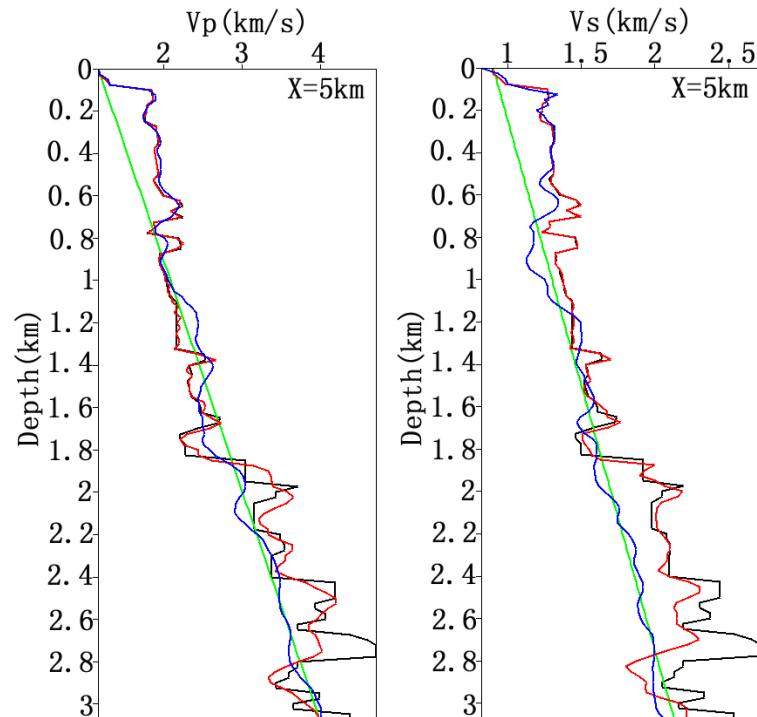


Figure 19. Comparison between velocity profiles extracted from models recovered by conventional EFWI (blue line) and our method (red line) for V_p and V_s in the first test at the location of 5 km. Starting and true models are depicted with green and black lines, respectively.

Elastic envelope inversion using multicomponent seismic data without low frequency

C. Huang et al.

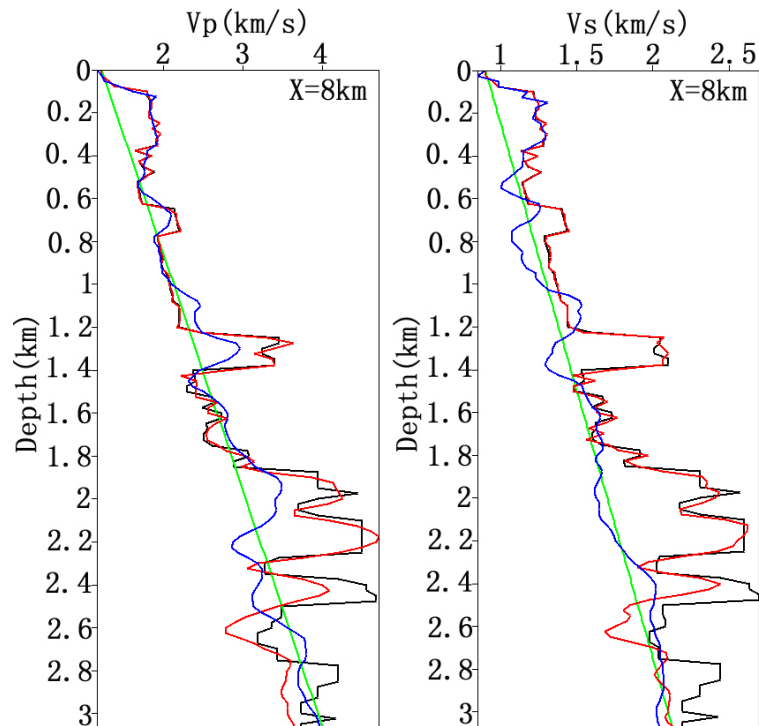
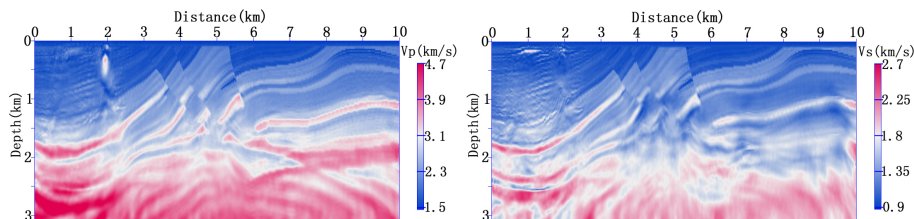


Figure 20. Comparison between velocity profiles extracted from models recovered by conventional EFWI (blue line) and our method (red line) for V_p and V_s in the first test at the location of 8 km. Starting and true models are depicted with green and black lines, respectively.

Elastic envelope inversion using multicomponent seismic data without low frequency

C. Huang et al.

**Figure 21.** Results obtained by conventional EFWI method in the second test.[Title Page](#)[Abstract](#)[Introduction](#)[Conclusions](#)[References](#)[Tables](#)[Figures](#)[◀](#)[▶](#)[◀](#)[▶](#)[Back](#)[Close](#)[Full Screen / Esc](#)[Printer-friendly Version](#)[Interactive Discussion](#)

Elastic envelope inversion using multicomponent seismic data without low frequency

C. Huang et al.

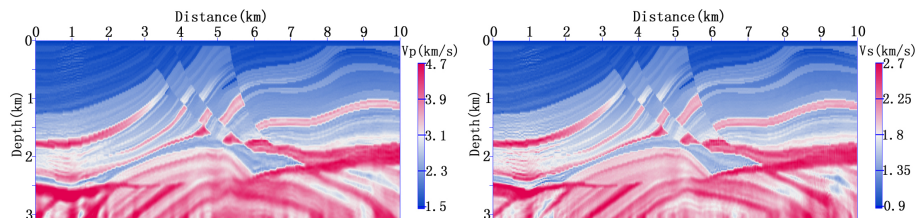


Figure 23. Final results after our two-step inversion in the second test.

[Title Page](#)[Abstract](#)[Introduction](#)[Conclusions](#)[References](#)[Tables](#)[Figures](#)[⏪](#)[⏩](#)[◀](#)[▶](#)[Back](#)[Close](#)[Full Screen / Esc](#)[Printer-friendly Version](#)[Interactive Discussion](#)

Elastic envelope inversion using multicomponent seismic data without low frequency

C. Huang et al.

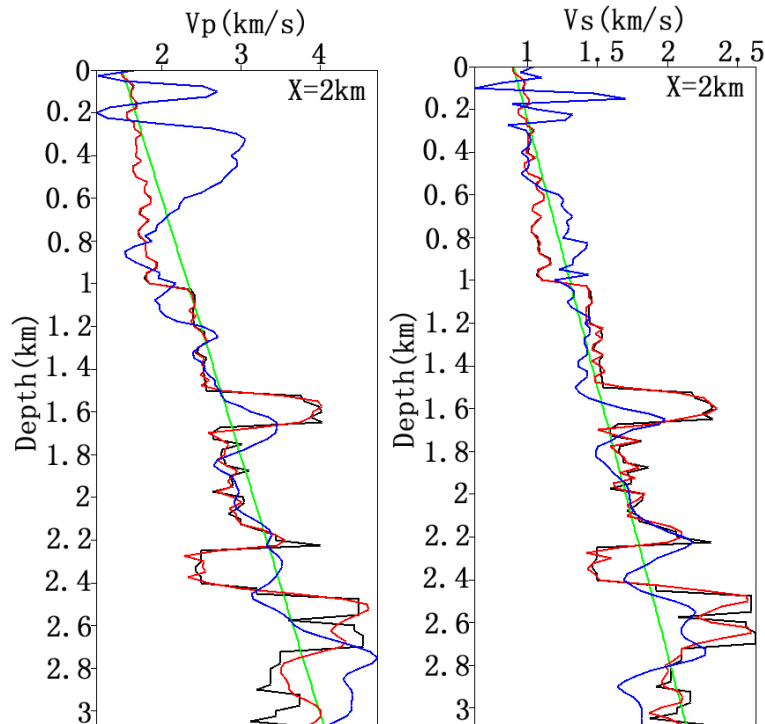


Figure 24. Comparison between velocity profiles extracted from models recovered by conventional EFWI (blue line) and our method (red line) for V_p and V_s in the second test at the location of 2 km. Starting and true models are depicted with green and black lines, respectively.

Elastic envelope inversion using multicomponent seismic data without low frequency

C. Huang et al.

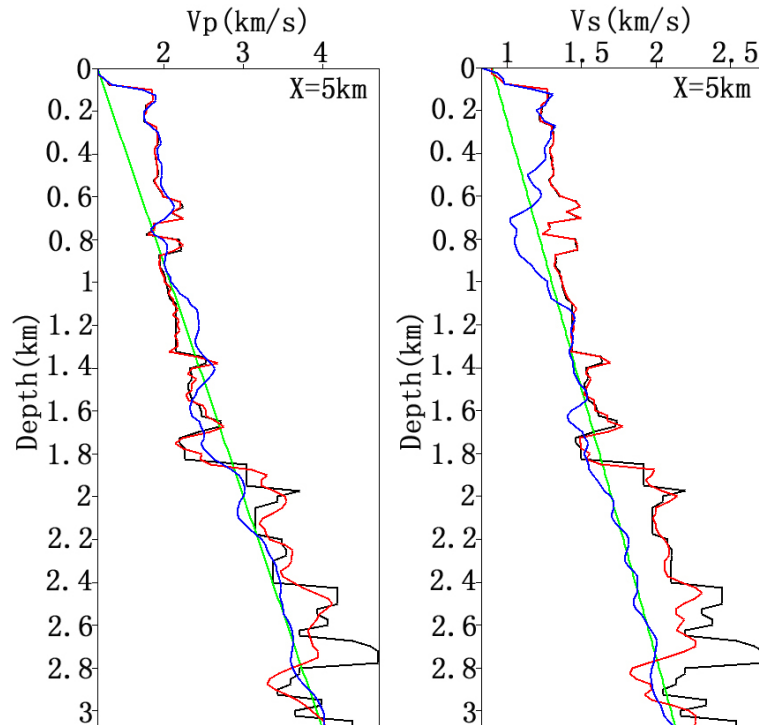


Figure 25. Comparison between velocity profiles extracted from models recovered by conventional EFWI (blue line) and our method (red line) for V_p and V_s in the second test at the location of 5 km. Starting and true models are depicted with green and black lines, respectively.

Elastic envelope inversion using multicomponent seismic data without low frequency

C. Huang et al.

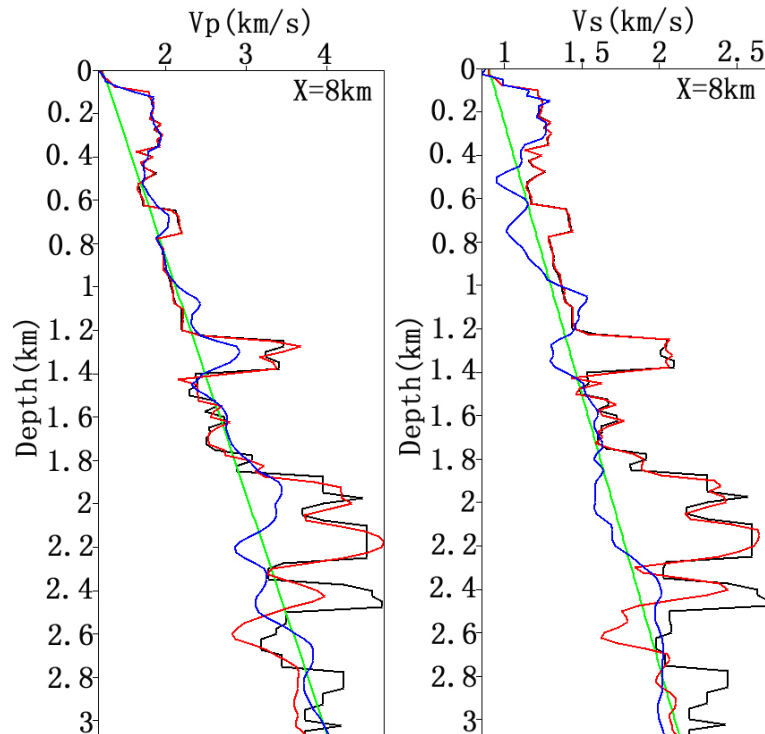


Figure 26. Comparison between velocity profiles extracted from models recovered by conventional EFWI (blue line) and our method (red line) for V_p and V_s in the second test at the location of 8 km. Starting and true models are depicted with green and black lines, respectively.